

Ionic conductivity and optical properties of self-activated phosphor CsYP207

mayssa karray (✉ mayssakarray@gmail.com)

University of Sfax

A. OUESLETI

University of Sfax

K. KHIROUNI

University of Sfax

M. GARGOURI

Gabes University

Research Article

Keywords: CsYP207, Optical properties, Impedance spectroscopy, Ionic conductivity, Modulus

Posted Date: August 18th, 2020

DOI: <https://doi.org/10.21203/rs.3.rs-61216/v1>

License: © ⓘ This work is licensed under a Creative Commons Attribution 4.0 International License.

[Read Full License](#)

Ionic conductivity and optical properties of self-activated phosphor CsYP₂O₇

M. KARRAY*, A. OUESLETI, K. KHIROUNI, M. GARGOURI

Laboratory of Spectroscopic Characterization and Optic Materials, University of Sfax, Faculty of Sciences of Sfax, B.P. 1171, 3000 Sfax, Tunisia.

Laboratory of Physics of Materials and Nanomaterials Applied at Environment, Faculty of Sciences in Gabes, Gabes University, 6072, Gabes, Tunisia

*: Corresponding author: mayssakarray@gmail.com

Abstract

Pyrophosphates are interesting compounds as optical materials, ionic conductors, solid electrolytes, battery electrodes, solid-state lasers and active layer for sensors. In this context, the compound CsYP₂O₇ has been synthesized by the solid-state reaction method. The X-ray powder diffraction at room temperature confirmed the phase formation of the synthesized compound in the monoclinic phase. The composition and morphology were performed by energy dispersive spectroscopy coupled with scanning electron microscope. The optical properties of the compound were studied by UV–Vis absorption spectroscopy. By direct investigation of the UV absorption measurements and using the Tauc model, we have found that the direct optical band gap is equal to 3.7 eV. Two of the relaxation mechanisms were clearly identified from Nyquist plots and modulus analysis, which can be discerned to both grain and grain boundary contributions effect. The obtained results were analyzed by fitting the experimental data to an equivalent circuit model. Bulk resistance and grain boundary resistance decreased with the increase of temperature, which confirmed negative temperature coefficient of resistance behavior. The same values of activation energies obtained from the impedance (0.43 eV) and hopping frequency (0.42 eV), prove that the transport happens through an ion hopping mechanism dominated by the motion of the Cs⁺ cations in the structure of the CsYP₂O₇ material. The results confirm that the synthesized compound is suitable for catalysis and optoelectronic applications.

Keywords: CsYP₂O₇, Optical properties, Impedance spectroscopy; Ionic conductivity; Modulus.

1. Introduction

In past years, pyrophosphates with general formula AMP_2O_7 ($A = Na, K, Rb, Cs$; $M = I, Ga, Fe, Cr, Y$) have extensively studied, due to the possibility of using these compounds as optical materials, ionic conductors, solid electrolytes, battery electrodes, solid-state lasers materials and sensors [1-7]. This family of compound shows a variety of structure types that are controlled by the stereo-chemical behaviors of the A and M cations. Besides, these cations affect the coordination numbers, the degree of distortion of the coordination polyhedra, and the conformation of the P_2O_7 groups [8-14]. In addition, the monovalent ions are responsible for the ionic conductivity properties that are observed in many compounds, with the attendant promise of applications such as solid electrolytes in rechargeable batteries [15–20]. The architecture of these pyrophosphates reflects a strong relationship between the crystal structure and physical properties. Recently, we have reported the electrical conduction mechanism of the MYP_2O_7 ($M = Na$ and Li) [21, 22]. Another interesting diphosphates, is $CsYP_2O_7$ compound with tunnel structure where the Cs^+ cations reside. We prepared this compound and we analyzed its crystalline structure. We found that it crystallizes in the monoclinic system (space group $P21/c$) with lattice parameters: $a = 7.897$ (3) Å, $b = 10.904$ (2) Å, $c = 8.758$ (1) Å, $\beta = 104.316$ (5)° [23]. Their structural arrangement consists of YO_6 octahedron which shares its six corners with six different P_2O_7 groups. Cs^+ cations are engaged in the intersecting tunnels formed by the alternate stacking of octahedral and phosphate layers (Fig. 1). This behavior is a good character to supply a good ionic conductivity [24].

Hence, the optical properties were studied by the analysis of the absorbance and reflectance spectra in UV-Vis range. Finally, the AC conductivity was studied to understand the conduction process in this material, via impedance spectroscopy in a wide range of frequencies and temperatures.

2. Synthesis and experimental

Elaboration of $CsYP_2O_7$ compound was achieved by solid-state reaction from pure reagents: Cs_2CO_3 , Y_2O_3 and $NH_4H_2PO_4$. All the precursors are of a purity higher than 99%. They were ground together in an agate mortar to attain a well homogeneous mixture. The obtained mixture was heated at 673 K for 8 h to dislodge NH_3 , CO_2 and H_2O . After that, the sample

was ground again, pressed to cylindrical pellets, and heated once more for 10 h at 973 K. Finally, the prepared pellets were sintered at 1073 K for 3 h.

X ray diffraction (XRD) pattern of the material was recorded at room temperature using a Phillips powder diffractometer operating with copper radiation ($\lambda = 1.5418 \text{ \AA}$) in a wide range of Bragg angles ($10^\circ \leq 2\theta \leq 60^\circ$).

Chemical analysis of samples in the form of pellets was carried out by EVO LS10 (Zeiss) scanning electron microscopy connected with energy dispersive system: INCA (Oxford Instruments).

The infrared spectrum was recorded, using an FTIR 100 PerkinElmer spectrophotometer, in the $1300 - 400 \text{ cm}^{-1}$ spectral range.

The optical absorption spectrum of sample was measured at room temperature using a UV-Vis spectrophotometer (SHIMADZU UV3100S) in the wavelength range of 200 – 800 nm.

The electrical measurements were performed using a two gold-electrode configuration. The powder was pelletized in a cylindrical shape with a typical diameter of 7 mm and thickness of 1.15mm and pressed at a pressure of 5 t/cm^2 . Electrical measurements were performed using 1260 Solartron Impedance Analyser automatic bridge monitored by a microcomputer in the temperature and frequency range 573-723 K and 200 Hz to 5 MHz, respectively.

3. Results and discussion

3.1. X-Ray Diffraction analysis

Room temperature XRD pattern of the CsYP_2O_7 compound is shown in Figure 2. The structural refinement was carried using Celref software based on Rietveld method. After several stretching, the several reflection peaks were indexed in the monoclinic symmetry with $P2_1/c$ space group. The lattice parameters were found to be $a = 7.897 (3) \text{ \AA}$, $b = 10.904 (2) \text{ \AA}$, $c = 8.758 (1) \text{ \AA}$, $\beta = 104.316 (5)^\circ$. The unit cell parameters of the material are in good agreement with the values found in the literature [23].

3.2. Scanning electron microscope analysis

Typical scanning electron microscope (SEM) micrographs of CsYP_2O_7 prepared by solid-state reaction are shown in Figure 3. The micrographs show small and bi grains. The smaller grain size are in the order of 10 nm and we note the appearance of these particles with same shape and unequal size. A statistical count of grain size was performed on SEM images using the Image J software. The results are expressed in the form histograms in Figure 4 as grain

number (counts) versus particle size. According to this figure, the obtained particles sizes are mainly in the order of 5 – 25 nm. This very small sizes of particle less than 1 μm indicates success and sensation of micro-particle synthesis [25]. In addition the Lorentzian fit shows that Cs and Y are distributed equally over the whole sample. Thus the structure is an average of homogeneous compositions.

3.3. Infrared spectroscopy

Figure 5 shows the infrared spectrum of the CsYP_2O_7 sample recorded at room temperature. The assignment of the bands was performed by comparison with similar compounds [22, 26-32]. The principal modes are assigned in the internal modes of the P_2O_7 group on the basis of the characteristic vibrations of the P–O–P bridge and PO_3 groups. We can observe three groups of bands. The first one is located in the region $(1257 - 1015) \text{ cm}^{-1}$ which is attributed to the symmetric and antisymmetric stretching modes of vibration (PO_3). The second one is in the range $(928 - 683) \text{ cm}^{-1}$ which corresponds to the symmetric and antisymmetric stretching modes of (POP). The third one is observed in the $(623 - 416) \text{ cm}^{-1}$ and they regions are attributed to the symmetric and antisymmetric of $\delta(\text{PO}_3)$ deformation modes. The band assignment for the fundamental modes of this compound, given in Table 1, confirms the presence of the diphosphate groups in the title compound.

3.4. Conductivity analysis

The Nyquist plot ($-Z''$ vs Z') is used to resolve the resistance (R) and capacitance (C) of the equivalent circuit associated with the grain and grain boundary, to evidence the polarization mechanism and to reflect the relaxation process. The inhomogeneity in the grain size of the ceramic materials results in the complex impedance diagram forming a tilted semicircular arc inclined to the relaxation for each of these contributions. Figure 6 shows the complex impedance data of the CsYP_2O_7 compound at various temperatures (623 – 723 K). This plots are fitted using an equivalent circuit formed by a series combination of two cells; the first was obtained by connecting in parallel a pure resistance (R_g) with a fractal capacitance constant phase element (CPE_g) corresponding to grain, whereas the second is formed by a parallel combination of a resistance (R_{gb}) with a pure capacitance (C_{gb}) and a fractal capacitance (CPE_{gb}) related to grain boundary.

The electrical conductivity spectroscopy is a well established method for characterizing the hopping dynamics of the charges carriers. The conductivity of bulk and grain boundary was calculated from Eqs. 1 and 2:

$$\sigma_g = \frac{e}{S \times R_g} \quad (1)$$

$$\sigma_{gb} = \frac{e}{S \times R_{gb}} \times \frac{C_g}{C_{gb}} \quad (2)$$

where, e is sample thickness, S is cross-sectional area, R_g is bulk resistance, R_{gb} is grain boundary resistance, C_g and C_{gb} are, respectively, the capacitance of grain and grain boundary. The pure capacitance C_{gb} is obtained from the constant phase element CPE, using the following equation:

$$C_{gb} = R_{gb}^{(1-\alpha)/\alpha} \times Q^{1/\alpha} \quad (3)$$

Where Q indicates the value of the capacitance of the CPE element and α is the degree of deviation with respect to the value of the pure capacitor.

Figure 7 presents the simulated Nyquist plot with equivalent circuit elements at 633 K. The experimental and the calculated data are in good agreement, indicating that the adopted equivalent circuit describes well the electrical properties of the title compound.

Figure 8 reported the variation of $\ln(\sigma_{g, \text{ and } gb})$ versus $1000/T$ for grains and grain boundaries. The linearity of $\ln(\sigma_{g, \text{ and } gb})$ versus $1000/T$ indicates that investigated material does not presents any phase transition in the studied temperature range. Furthermore the conductivity $\sigma_{g, \text{ and } gb}$ obeys the Arrhenius law [33]:

$$\sigma_{g, gb} = \sigma_{0g, gb} \exp\left(-\frac{E_{ag, gb}}{K_B T}\right) \quad (4)$$

Where $\sigma_{g, \text{ and } gb}$ is electrical conductivity, $\sigma_{0g, \text{ and } gb}$ is the pre-exponential factor, T is temperature, K_B is the Boltzmann constant and $E_{ag \text{ and } gb}$ are the activation energies..

The activation energies obtained from the Arrhenius plot, are indicated in Figure 8. The activation energies obtained both from bulk and grain boundary are nearly the same. This behaviors indicates that the conduction of the grain and the grain boundary increases at a similar rate with an increase in temperature.

The obtained activation energies E_{ag} and E_{agb} are similar to those reported for semiconductor compounds [29, 34]. Comparing to other diphosphates compound (Table 2), this low activation energy can be attributed to a lower Cs^+ radii. Other-wise, it is also related to the dimension of the tunnels in $CsYP_2O_7$.

Figure 9 shows that the semi-logarithmic variation of total conductivity (σ_{ac}) as a function of frequency presents two regions: the first is an independent low frequency domain (the presence of plateau), which refers to direct current conductivity (σ_{dc}) due to the long-range movement of free charge [36]. The second region of σ_{ac} curve, we observe an increase of conductivity as a function of frequency. Consequently, the AC conductivity equation can be described by the known universal Jonscher power law [37]:

$$\sigma_{ac}(\omega) = \sigma_{dc} + A\omega^s \quad (5)$$

Where (σ_{dc}) is the value of direct current conductivity A is a constant that is temperature dependent, and s is power law exponent, where $0 < s < 1$. s represents the degree of interaction between mobile ions with the environments surrounding them, and A determines the strength of polarizability. The change in the behavior of σ_{ac} occurs at the hopping pulsation ω_h . The activation energy calculated from the slope of $\ln(\omega_h)$ versus $1000/T$ (Figure 9 Inset) is found to be $E_{ah} = (0.43 \pm 0.05)$ eV. This value is closely to that E_{ag} determined above from conductivity against the inverse of temperature. This result suggests that the mobility of the charge carriers is due to a hopping mechanism, assured by Cs^+ cations' hopping in tunnels along c-axis tunnels [38].

View of the shape and size of the [001] tunnel sections is presented in Figure 10 using DIAMOND-Visual Crystal Structure software, which shows that the only conduction pathway is along tunnels in the c-direction, and the modest conductivity is determined by the dimensions of the tunnels section where Cs^+ cations are located. Moreover, the dimensions of the tunnels vary between 5.138 \AA and 8.016 \AA , while, according to Shannon radii, the diameter of the cesium ion is 3.62 \AA [39]. So this tunnel is of a sufficient dimension for ion transport. Thus, it can be deduced that the conduction process is assured by the movement of the Cs^+ cations along c-axis tunnels.

3.5. Electric modulus analysis

The formalism modulus is an important tool to justify electrical relaxation behavior in ion conducting material and is useful to understand the bulk responses of material as electrode polarization effect are minimized. The complex electric modulus M^* can be represented by the following equation [40]:

$$M^*(\omega) = \frac{1}{\epsilon^*(\omega)} = j\omega C_0 Z^*(\omega) \quad (6)$$

Where ϵ^* is complex permittivity and C_0 is vacuum capacitance of the cell.

The curves reflecting the variation of the imaginary part as a function of ω for different temperatures are given in Figure 11. At a given temperature, these spectra show two asymmetric relaxation peaks. The peak at low frequency is related to the grains boundaries effects, the second observed at high frequency is correlated to the grains.

At the low-frequency region, M'' spectrum indicates that the charge carriers are mobile over long distances from one site to a neighboring site, while in the high-frequency region, the carriers were spatially confined in potential wells and become mobile over a short distance. This is correlated to thermally activated transition of conductive mechanism from long range to short range type hopping of charge carriers [41].

The double peak feature is fitted by using the well known Bergman equation [42]. The fit values of β_g parameter related to the grain contribution remains in the vicinity of 0.86 when the temperature varies. So, the values of β_g ($\beta_g < 1$) and the asymmetric peaks propose a non-Debye-type dielectric relaxation [43]. The nature of modulus curves indicates that the electrical conduction of the studied materials is described by the hopping mechanism.

Further the angular frequency ω_{max} of the peak maximum (related to the relaxation time τ) is plotted as inverse function of temperature ($1000/T$) and shown in Figure 12. The insert value gives the calculated activation energies by using the Arrhenius law (eq. 4). The calculated activation energy from a linear fit to the data points is the activation energy for bulk and grain boundary are about $E_{mg} = (0.43 \pm 0.05)$ eV and $E_{mgb} = (0.39 \pm 0.05)$ eV, respectively. The activation energy E_{mg} and E_{ag} obtained respectively from the conductivity relaxation time and the hopping pulsation are very closely, suggesting that the relaxation process and the electrical conductivity are ascribed to the same effect and it indicates that ions have to overcome the same barrier while conducting as well as when relaxing.

3. 6. Optical properties

Generally, ultraviolet–visible (UV–Vis) spectroscopy was used to investigate the change in the optical energy gap, the absorption coefficient (α), and the Urbach energy. The absorbance spectrum of CsYP₂O₇ was performed at room temperature in the wavelength range (200–800nm). This spectrum, as represented in Figure 13, appears to have multiple contributions, which were obtained by a deconvolution of the parent spectrum into 4 spectra by Gaussian fitting.

Firstly, the UV-Vis spectrum exhibits two broad bands (200 – 250 nm) dominating the short wavelength region of absorbance spectrum. The band with shorter wavelength can be assigned as the inter-band transition (valence band to conduction band) of CsYP₂O₇ [44, 45]. The other band with longer wavelength can be assigned as a conduction band charge transfer (CT) de type B with maximum at 248 nm, due to the CT absorption of O²⁻– Y³⁺ [46, 47].

Secondly, from 250 to 500 nm, the obtained spectrum exhibit four absorption peaks precisely at 274, 311, 382, 489 nm. The both observed band at 274 nm (4.52 eV) and 311 nm (3.98 eV) are due to the ⁸S_{7/2} to ⁶I_{7/2}, and ⁸S_{7/2} to ⁶P_{7/2} transition of Y³⁺ [48], respectively. While, the other both band at 382 and 489 nm (3.24 eV – 2.53 eV) are attributed to ⁵D₃ to ⁷F₆ and ⁵D₄ to ⁷F₆ transition, respectively. The origin of that low energy absorbance band, can be attributed to energy transfer Y³⁺ – Y³⁺ and to origin from Y– pair or clusters [49].

Compared these results obtained with the literature, CsYP₂O₇ is a suitable compound for doping with rare earth activators due to the optical inactivity of Y³⁺ ions, which can be easily substituted by trivalent lanthanide.

The inset of Figure12 shows the UV-Vis diffuse reflectance spectrum of the CsYP₂O₇, where the broad band in the spectral range of ~200-360 nm can be assigned to absorption by the CsYP₂O₇ host. It is agree with the absorbance spectrum. In addition this spectrum is the same to Na₂YPO₄ and Sr₃YP₃O₁₂ compound [50, 51].

The relation between the absorption coefficient, the energy band gap E_g and the coefficient (n) associated to an electronic transition is given by the Tauc equation [52]:

$$(\alpha h\nu)^n = A_1(h\nu - E_g) \quad (7)$$

where $h\nu$ means the energy of photon, A_1 is an energy-independent constant called band tailing parameter and E_g represents the value of the band gap, $n = 1/2$ stands for indirect allowed transition, 2 means a direct allowed transition, $3/2$ represents a direct forbidden transition, or $1/3$ indicates an indirect forbidden transition. Therefore, Figure14 shows the variation of $(\alpha h\nu)^2$ and $(\alpha h\nu)^{1/2}$ versus the photon energy. The band gap energy is estimated from the extrapolation of the straight line portion until the energy axis to be 3.7eV and 3 eV respectively. CsYP₂O₇ compound has optical properties, comparable to those found for other pyrophosphates, thus these materials can be classified as semiconductors [53, 54] (Table 3).

The inclusion of impurity in the semiconductor frequently make the formation of band tailing in the band gap due to the interaction of phonons. The Urbach energy characterizes the

disorder of a compound and corresponds to transitions between extended states of the valence band and localized states of the conduction band. This disorder in the compound can be deduce from the variation of the absorption coefficient α obtained by the Beer-Lambert relation:

$$\alpha = \alpha_0 \exp\left(\frac{h\nu}{E_u}\right) \quad (8)$$

where α_0 is the band tailing parameter and E_u is the Urbach energy estimated from the plot of $\ln(\alpha)$ versus $(h\nu)$. The determination of the tangent inverse to the inflection points of the fundamental and second transitions provides the Urbach energy as shown in Figure 15 which is about 0.32eV.

We notice the existence of an inverse variation between the gap energy and the Urbach energy. This inverse variation is logical because, the disorder is characterized by the tail width of valence band or conduction as well as the optical gap is the energy gap between the tails of bands. In addition, compared with the literature, the value proved the presence of a limited disorder [55].

4. Conclusion

In this present work CsYP₂O₇ compound was successfully prepared by solid state reaction. X-ray analysis revealed that this material crystallized with P2/c space group. The IR spectrum was interpreted on the basis of the structural peculiarities of the P₂O₇⁴⁻ moieties present in the sample.

Nyquist plots permitted to determine an equivalent electrical circuit. According to Arrhenius law, the activation energies deduced from conductivity, hopping frequency and relaxation time are close, signifying that the ionic transport in the CsYP₂O₇ compound is described by a hopping mechanism assured by Cs⁺ cations' hopping in tunnels which has a better activation energy compared with other diphosphates compound.

Secondly, by means of UV-Vis, the absorption spectra, exhibits two broad bands (160-250) nm, and four absorption peaks (250-500) nm. Each peak is assigned to a specific charge transition attached to the Y⁺. Then, we measured the direct (3.7 eV) and indirect gap energy (3 eV) and we determined the Urbach. These optics results obtained, shows that CsYP₂O₇ is a suitable compound for doping with rare earth activators due to the optical inactivity of

Y^{3+} ions. Finally, according to these important optical properties, $CsY_2P_2O_7$ phosphor material is dominating as laser materials, and suitable for solid-state lighting applications.

References

- [1] M.E. Hagerman, K. R. Poeppelmeier, *Chem. Mater.* 7 (1995) 602–621.
- [2] S. Nasri, A. Oueslati, I. Chaabane, M. Gargouri, *Ceram. Int.* 42 (2016) 14041–14048.
- [3] S. Nasri, A. Oueslati, I. Chaabane, M. Gargouri, *Ionics* 21(2015) 67–78.
- [4] Y. Ben Taher, A. Oueslati, M. Gargouri, *J. Alloys Compd.* 668 (2016) 206–212.
- [5] C.R. Mariappan, G. Govindaraj, S.V. Rathan, G.V. Prakash, *Mater.Sci. Eng. B* 123 (2005) 63–68.
- [6] K. Rissouli, K. Benkhoucha, J.R. Ramos, C. Julien, *Mater. Scie. Eng. B* 98 (2003), 185–189.
- [7] B. Louati, M. Gargouri, K. Guidara, T. Mhiri, *J. Phys. Chem. Solids* 66 (2004) 762 –765.
- [8] J.M. Le Meins, G. Courbion, *Acta Cryst. C*55 (1999) 481–483.
- [9] D. Rlou, H. Leligny, C. Pham, P. Labbe, B. Raveau, *Acta Cryst. B* 47 (1991) 608–617.
- [10] D.R. Adams, R. Layland, *Polyhedron* 14 (1995) 3473 –3480.
- [11] A. Moqine, A. Boukhari, L. Elammari, J. Durand, *J. Solid State Chem.* 107 (1993) 368–372.
- [12] A. Alaoui, E. Belghiti, A. Elmarzouki, A. Boukhari, E.M. Holt, *J. Solid State Chem.*109 (1994) 333–337.
- [13] K. Maa, R. Glaum, R. Gruehn, *Z. Anorg, Allg. Chem.* 627 (2001) 2081–2090.
- [14] F.Q. Huang and J. A. Ibers, *Acta Cryst. C*56 (2000) 625–626.
- [15] S. Villain, E. Nigrelli, G. Nihoul, *Solid State Ionics* 116 (1999) 73 –83.
- [16] K. H. Naifer, M. Ferid, *Solid State Ionics* 176 (2005) 1949–1953.
- [17] A. Béjaoui, K. H. Naifer, M. Férid, *J. Solid State Chem.* 204 (2013) 224–232.
- [18] A. Béjaoui, K. H. Naifer, M. Hajji, M. Férid, *Solid State Sci.* 31(2014) 46–53.
- [19] Y. Zhang, W. Cheng, D. Wu, H. Zhang, D. Chen, Y. Gong, Z. Kan, *Chem. Mater.* 16 (2004) 4150–4159.
- [20] J.L. Yuan, H. Zhang, H.H. Chen, X.X. Yang, J.T. Zhao, M. Gu, *J. Solid State Chem.* 180 (2007) 3381–3387.

- [21] A. Oueslati, M. Gargouri, *J. Electro.* 42 (2018) 129–135.
- [22] A. Oueslati, *Ionics.* 42 (2016) 129–135.
- [23] A. Akrim, D. Zambon and J.C. Cousseins, *J. Alloys. Comp.* 207/208 (1994) 99–101.
- [24] S.R. Elliott, *Advances In Physics* 36 (1987) 135 –218.
- [25] Y.Pu, Y. Huang, T. Tsuboi, H.Cheng, H.J. Seo, *RSC Adv.* 00 (2012) 1–3.
- [26] S. Nasri , M. Megdiche , M. Gargouri, *Physica B.* 451 (2014) 120–127.
- [27] S. Nasri, A. Oueslati, I. Chaabane, M. Gargouri, *Ceram. Int.* 42 (2016) 14041–14048.
- [28] M. Sassi, A. Oueslati, N. Moutia, K. Khirouni, M. Gargouri1, *Ionics* 23 (2017) 847–855.
- [29] S. Mathlouthi, A. Oueslati, B. Louati, *J. All. Comp.* **794** (2019) 417–424.
- [30] O. Ajili, B. Louati, K. Guidara, *Indian J Phys* 92 (2018) 875–881.
- [31] O. Ajili, B. Louati, K. Guidara, 119 (2015) 1119–1125.
- [32] N. Khay, A. Ennaciri, A. Rulmont, *J. Raman Spectrosc.* 32 (2001) 1052 –1058.
- [33] C.R. Mariappan, G. Govindaraj, S.V. Rathan, G.V. Prakash, *J. Mater. Sci. Eng. B1212* (2005) 8.
- [34] S. Mathlouthi, A. Oueslati, B. Louati, *Indian J Phys.* 93 (2019) 603–610.
- [35] S. Nasri, M. Megdiche, K. Guidara, M. Gargouri, *Ionics*, 19 (2013) 1921–1931.
- [36] K. Funke, *Pro S. Solid St Chem.* 22 (1993)111–195.
- [37] A. K. Jonscher, *Dielectric Relaxation in Solids* (1983)
- [38] A. Jouinia, J.C. Gâcona, M.Feridb, M.T. Ayadic , *Opt. Mat.* 24 (2003) 175–180.
- [39] R. D. Shannon, *Acta. Cryst. Sect. A32* (1976) 751–767.
- [40] H. Mahamoud, B. Louati,F. Hlel, K. Guidara, *J. All.Comp.* 509 (2011) 6083–6089.
- [41] R.N. Howmik, K.S. A. Kumar, *Mater. Chem. Phys.* 177 (2016) 417–428.
- [42] R. Bergman, *J. Appl. Phys.* 88 (2001)1356–1365.
- [43]A. Siaï, K. H. Naifer, M. Férid, *J. Appl. Phys.* 123 (2018) 035–105.
- [44] J.L. Yuan, X.J. Wang, D.B. Xiong, C.J. Duan, J.T. Zhao,Y.B.. Fu, G. B.Zhang, C. S. Shi, *J. Lum.* 126 (2007) 130–134.
- [45] A.M. Srivastava, S.J. Camardello, *Opt.Mat.* 39 (2015) 130–133.

- [46] L. Van. Pieterson, M.F. Reid, R.T. Wegh, S. Soverna, A. Meijerink, *Phy. Rev. B*, 65 (2002) 045–113.
- [47] D. Wanga, Y. Wanga, *Mat. Chem. Phy.* 115 (2009) 699–702.
- [48] M. Daoud, D. Zambon, R. Mahiou, A. Ammar, B. Tanouti, *Mat. Res. Bull.*, 33 (1998) 597–603.
- [49] A. Akrim, D. Zambon and J.C. Cousseins, *J.AL.COM*, 207/208 (1994) 99–101.
- [50] M. Daub, A.J. Lehnerb, H. A. Höpfe, *Dalton Trans.* 41 (2012) 12121–12128.
- [51] W. Liu, X. Wang, Q. Zhu, X. Li, X. Sun, J.G Li, *Sci. Tech. Adv. Mat.* 20 (2019) 949–963.
- [52] J. Tauc, *Amorphous and Liquid Semiconductors*, first ed., Plenum, London, 1974.
- [53] J.L. Yuan, H. Zhang, H.H. Chen, X.X. Yang, J.T. Zhao, M. Gu, *J. Solid State Chem.* 180 (2007) 3381–3387.
- [54] D. Zhaoa, F. Maa, R. Zhangb, R. Zhanga, L. Zhanga, Y. Fana, *Mat. Res. Bulletin* 87 (2017) 202–207.
- [55] B. Tbib, M. Eddy, K.El-Hami, *AIP Conference Proceedings* 1932 (2018) 030–042.

Tables:

Table 1: Assignment of IR bands for CsYP₂O₇ compound

Table 2: Activation energies, conductivity and conduction mechanism of yttrium diphosphate

Table 3: Gap energies of some rare earth compounds

Figures:

Figure 1: Projection parallel to the c direction of the structure of CsYP₂O₇ pyrophosphate

Figure 2: X-ray diffraction pattern of CsYP₂O₇ pyrophosphate

Figure 3: SEM images for CsYP₂O₇

Figure 4: Size distribution histogram with corresponding Lorentzian fit for CsYP₂O₇

Figure 5: IR spectra of CsYP₂O₇

Figure 6: The Nyquist plots for CsYP₂O₇ at different temperatures

Figure 7: Simulated Nyquist plot with equivalent circuit elements for CsYP₂O₇ at 633 K

Figure 8: Arrhenius plots for the grain and grain boundary conductivity

Figure 9: Variation of AC conductivity. Inset: Temperature dependence of the hopping frequency ω_h

Figure 10: View of the shape and size of the [001] tunnel sections

Figure 11: Imaginary part of the electrical modulus of the CsYP₂O₇

Figure 12: Temperature dependence of M''_{\max}

Figure 13: The absorbance and reflectance spectra for CsYP₂O₇ compound

Figure 14: Dependence of $(\alpha h\nu)^2$ and $(\alpha h\nu)^{1/2}$ on the photon energy of CsYP₂O₇ compound.

Figure 15: The logarithmic variation of the absorption coefficient versus photon energy

Figures

Figure 1

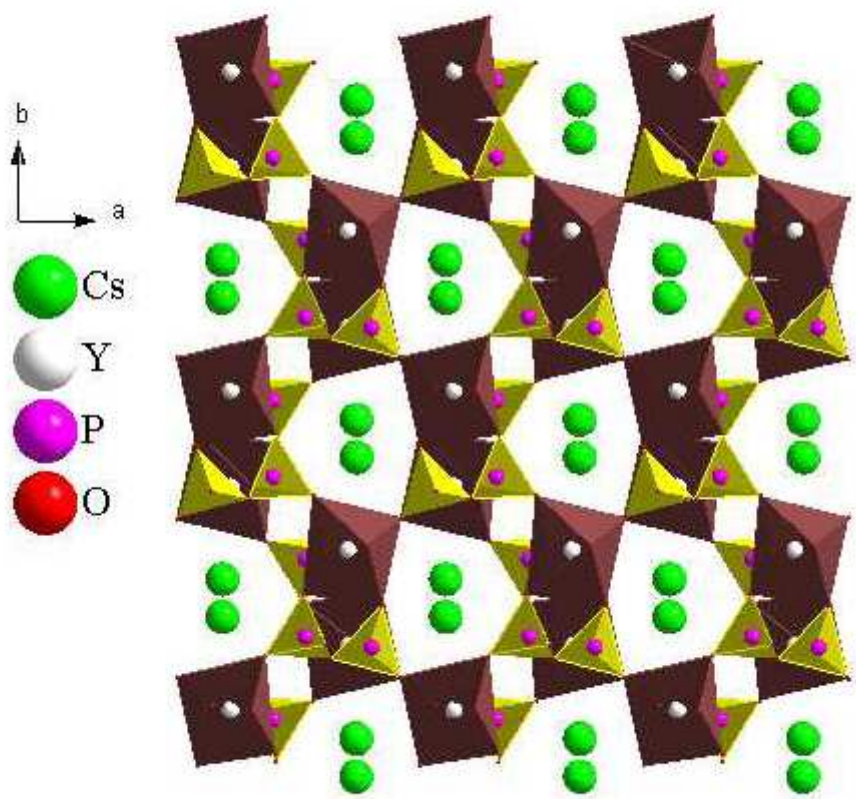


Figure 1

Projection parallel to the c direction of the structure of CsYP207 pyrophosphate

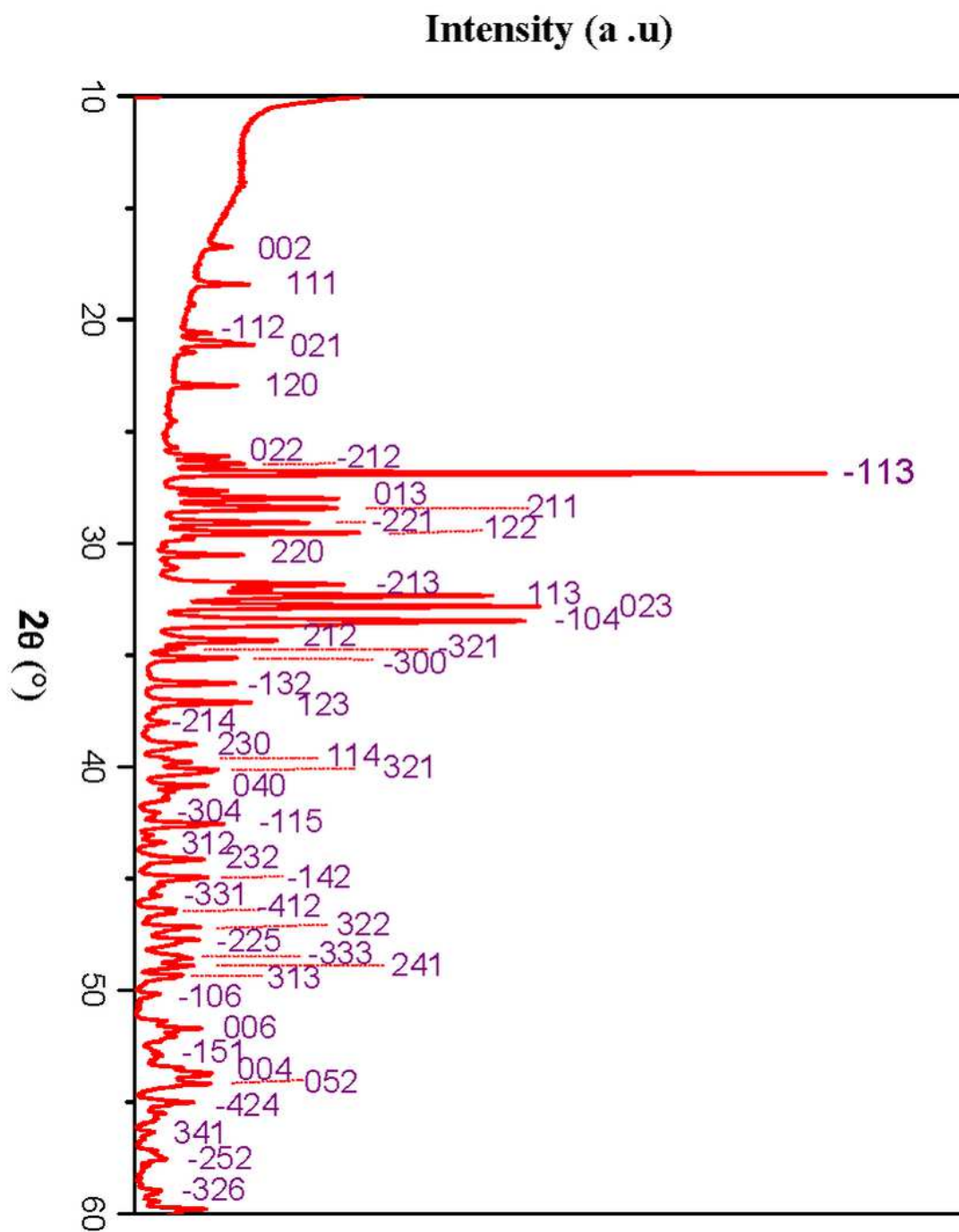


Figure 2

X-ray diffraction pattern of CsYP207 pyrophosphate

Figure 3

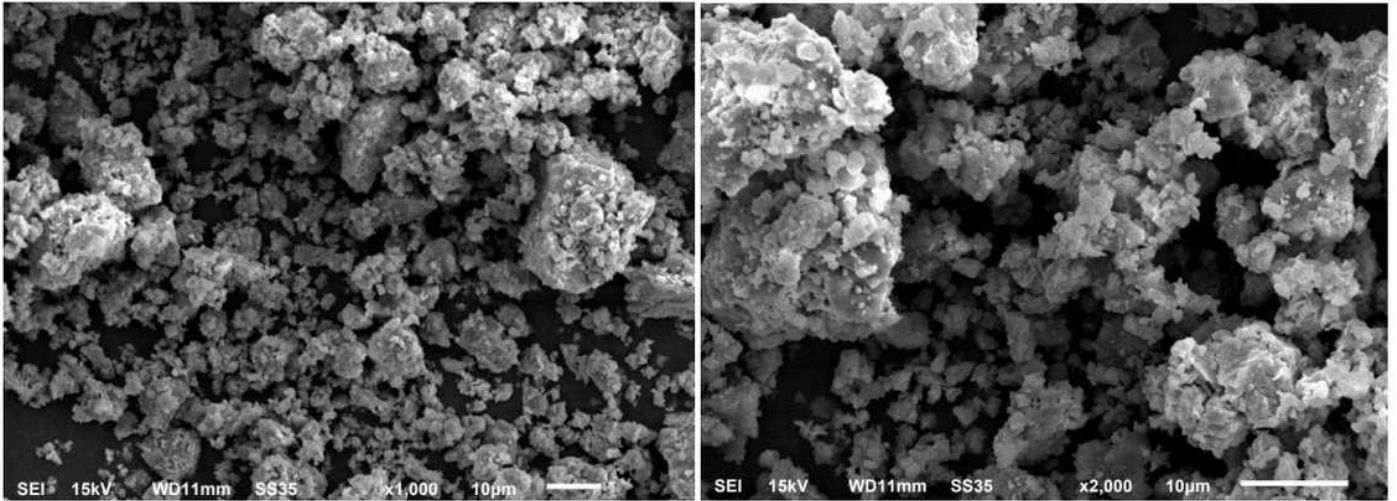


Figure 3

SEM images for CsYP207

Figure 4

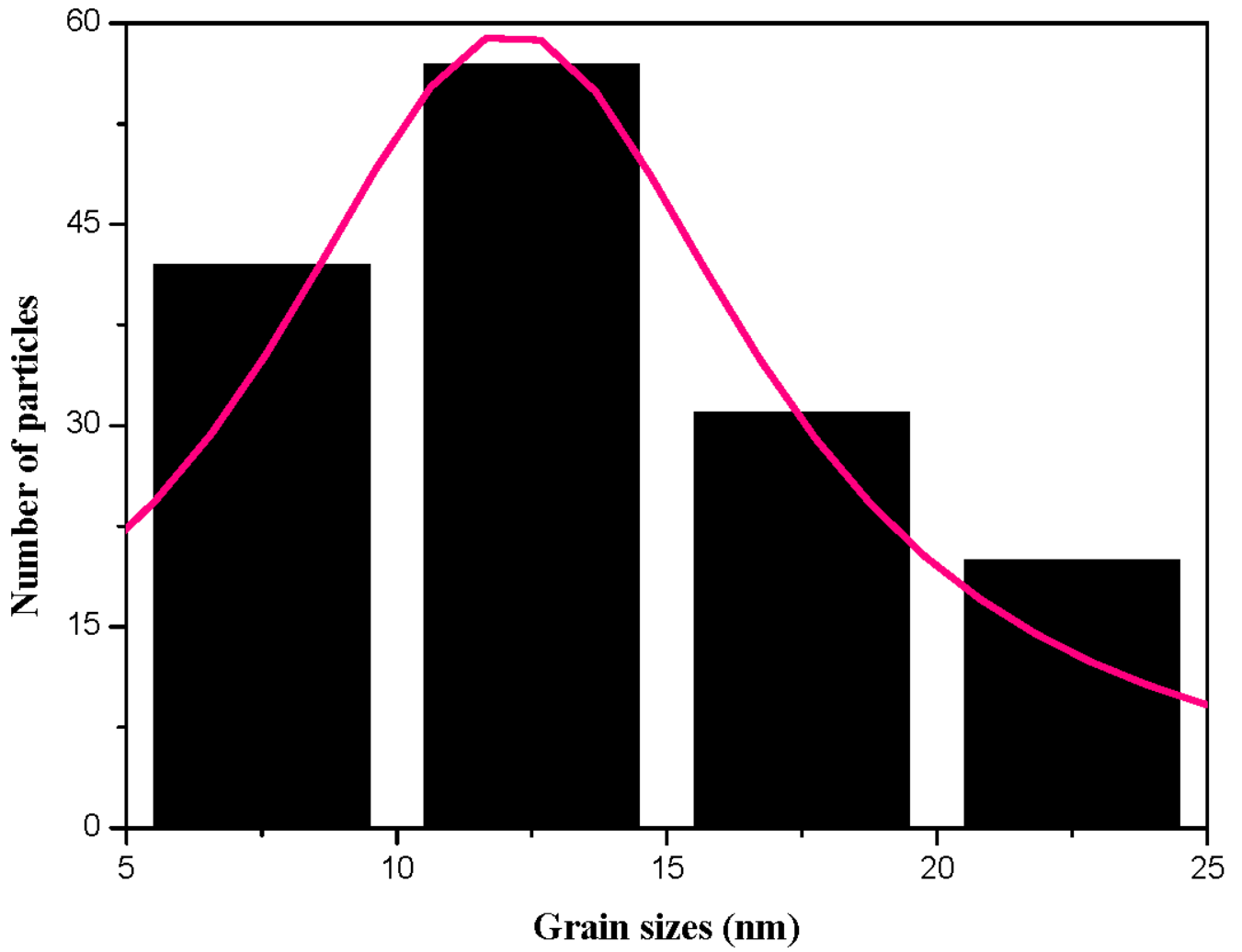


Figure 4

Size distribution histogram with corresponding Lorentzian fit for CsYP207

Figure 5

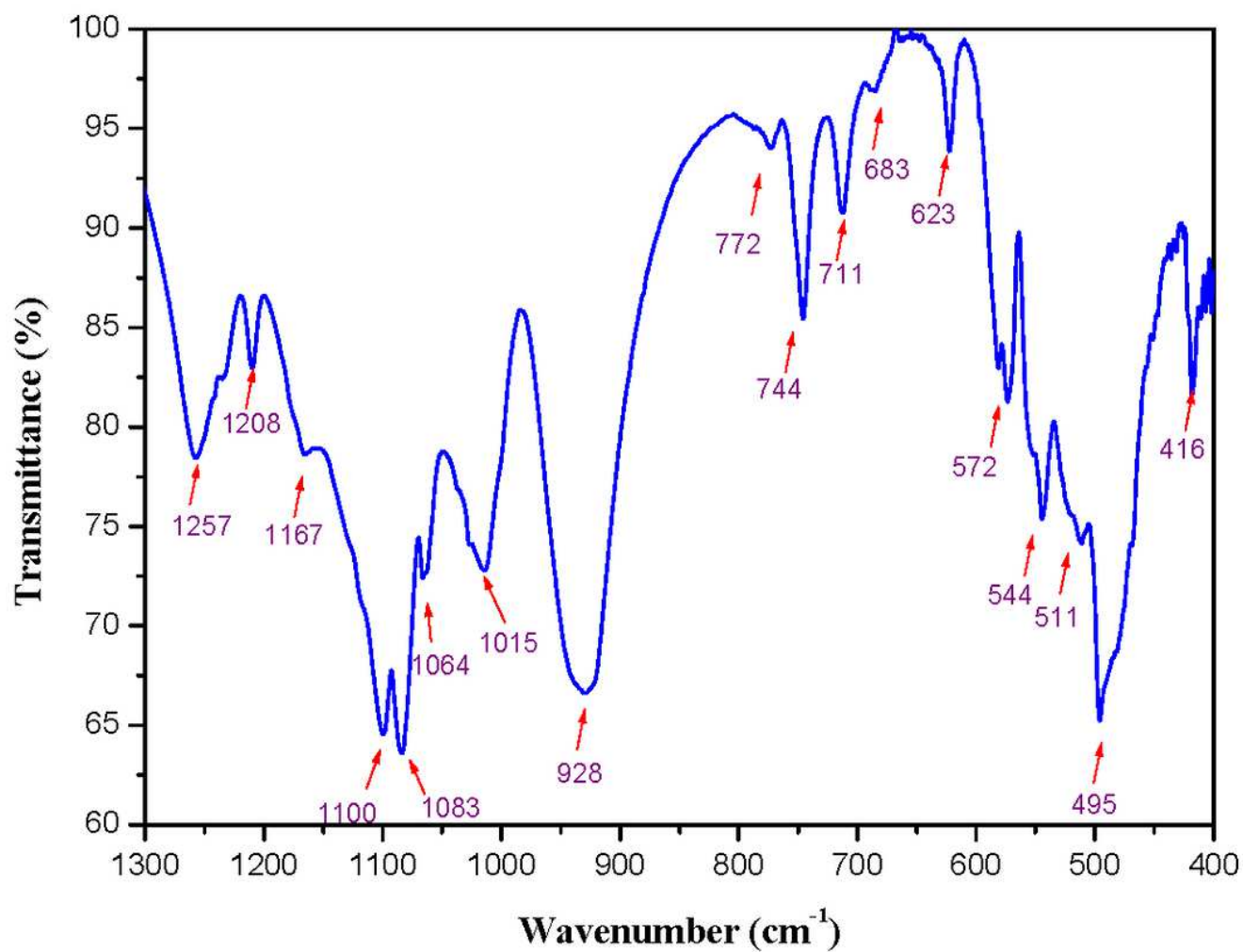


Figure 5

IR spectra of CsYP207

Figure 6

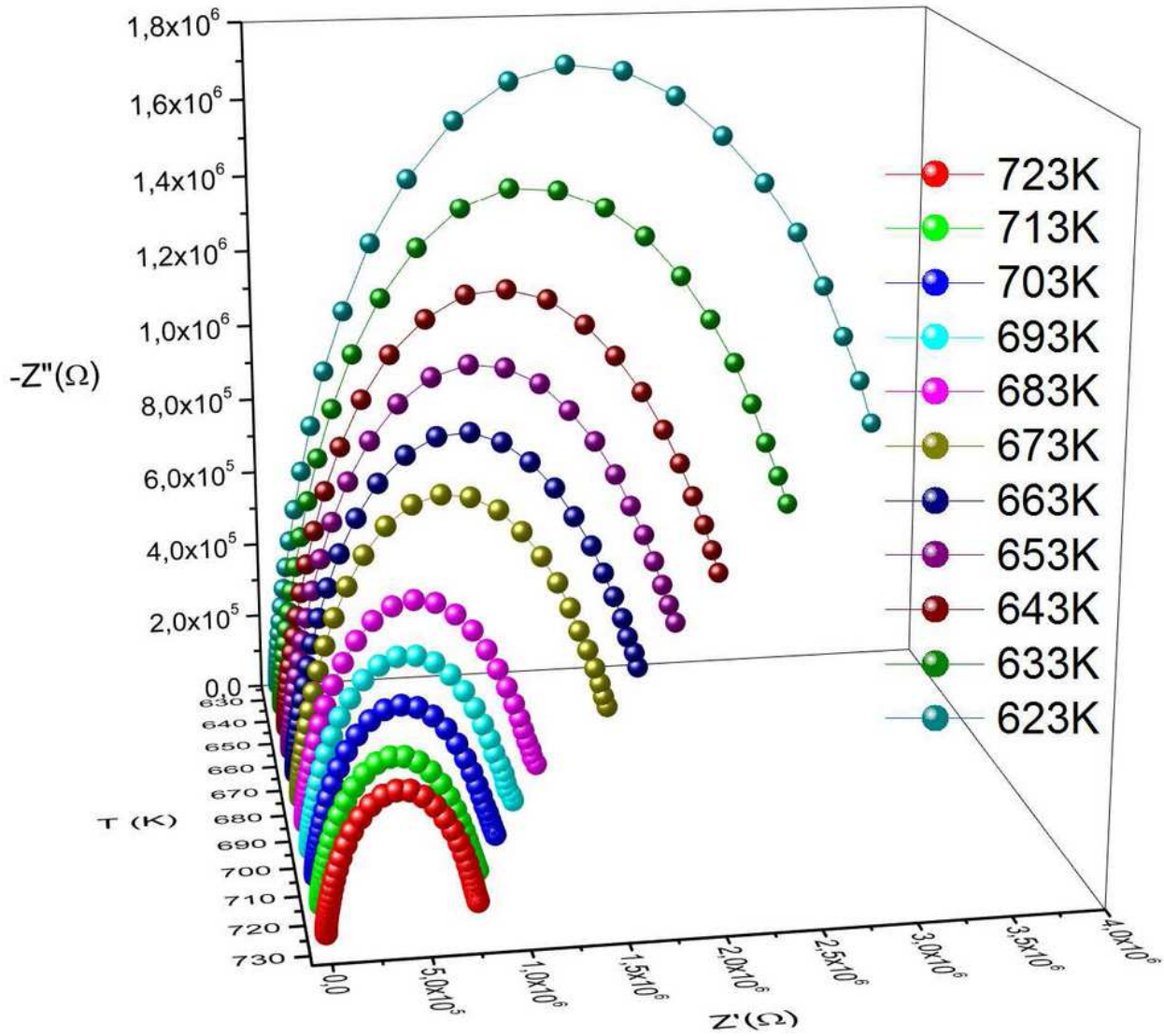


Figure 6

The Nyquist plots for CsYP207 at different temperatures

Figure 7

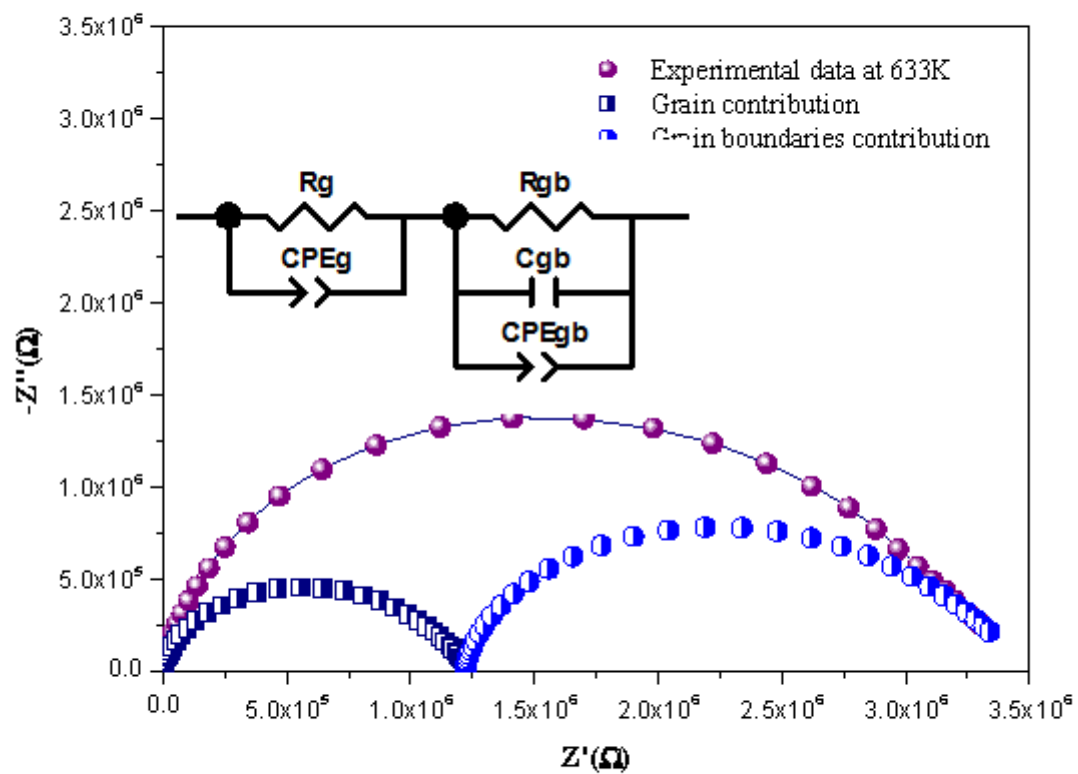


Figure 7

Simulated Nyquist plot with equivalent circuit elements for CsYP207 at 633 K

Figure 8

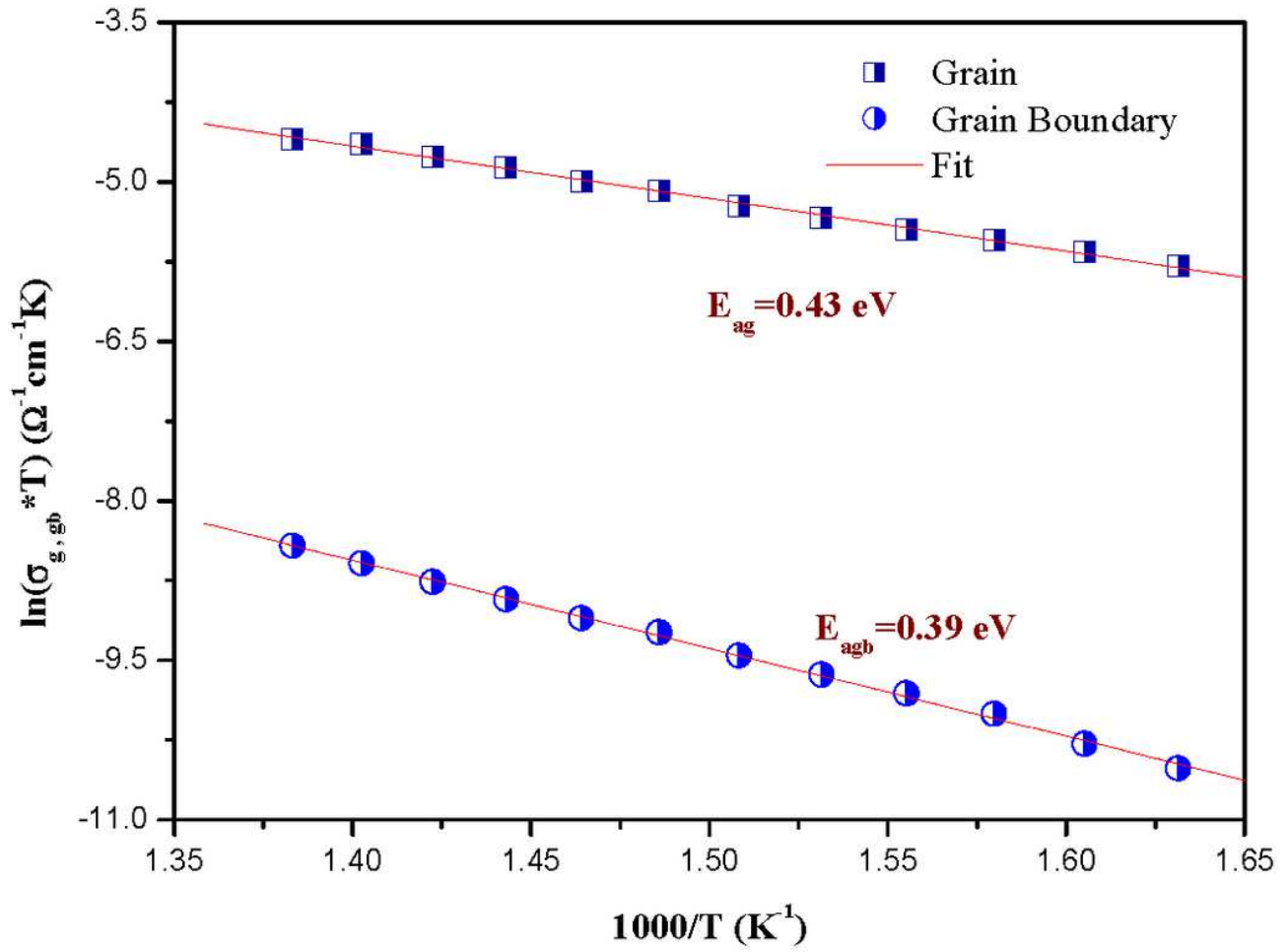


Figure 8

Arrhenius plots for the grain and grain boundary conductivity

Figure 9

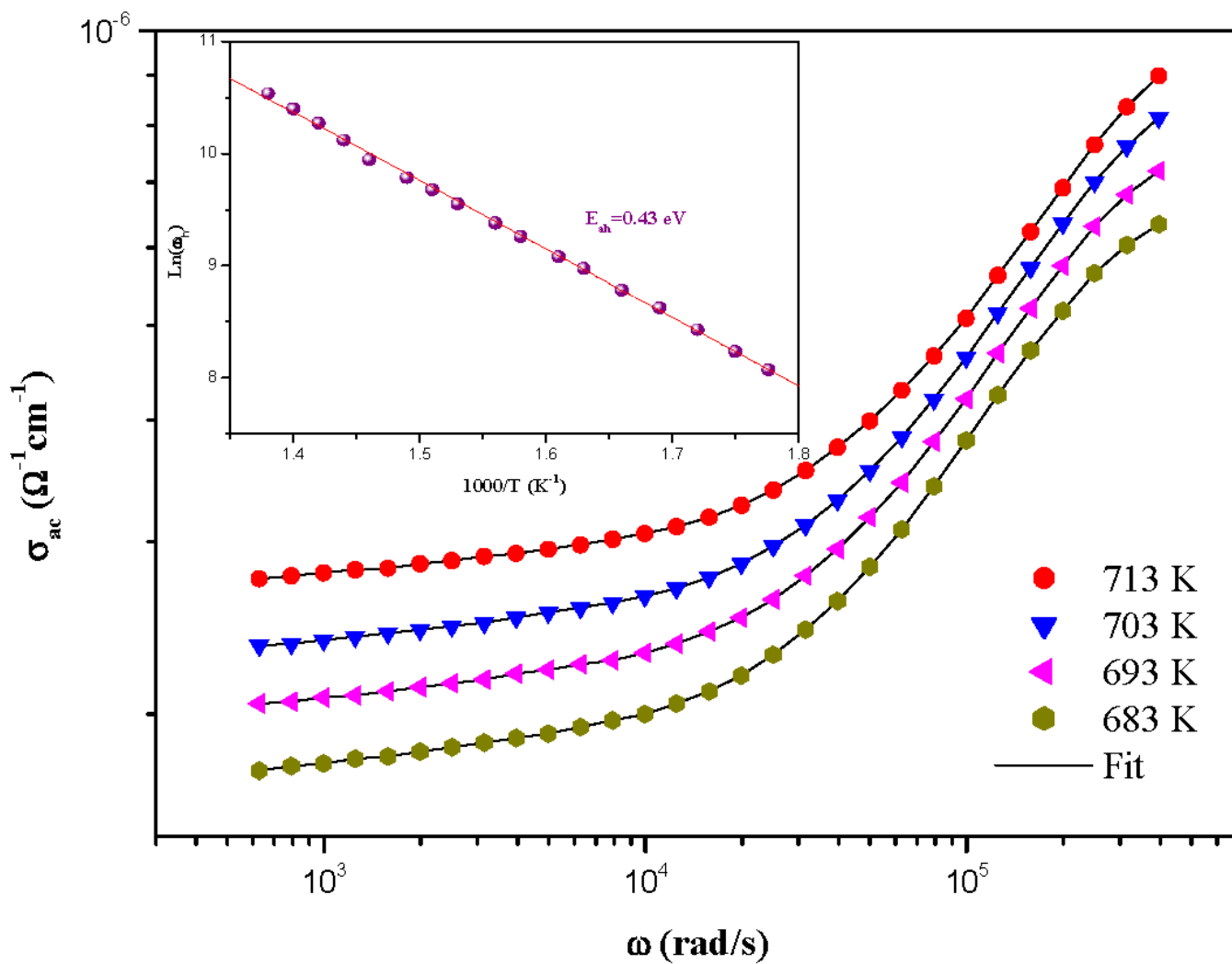


Figure 9

Variation of AC conductivity. Inset: Temperature dependence of the hopping frequency ω_h

Figure 10

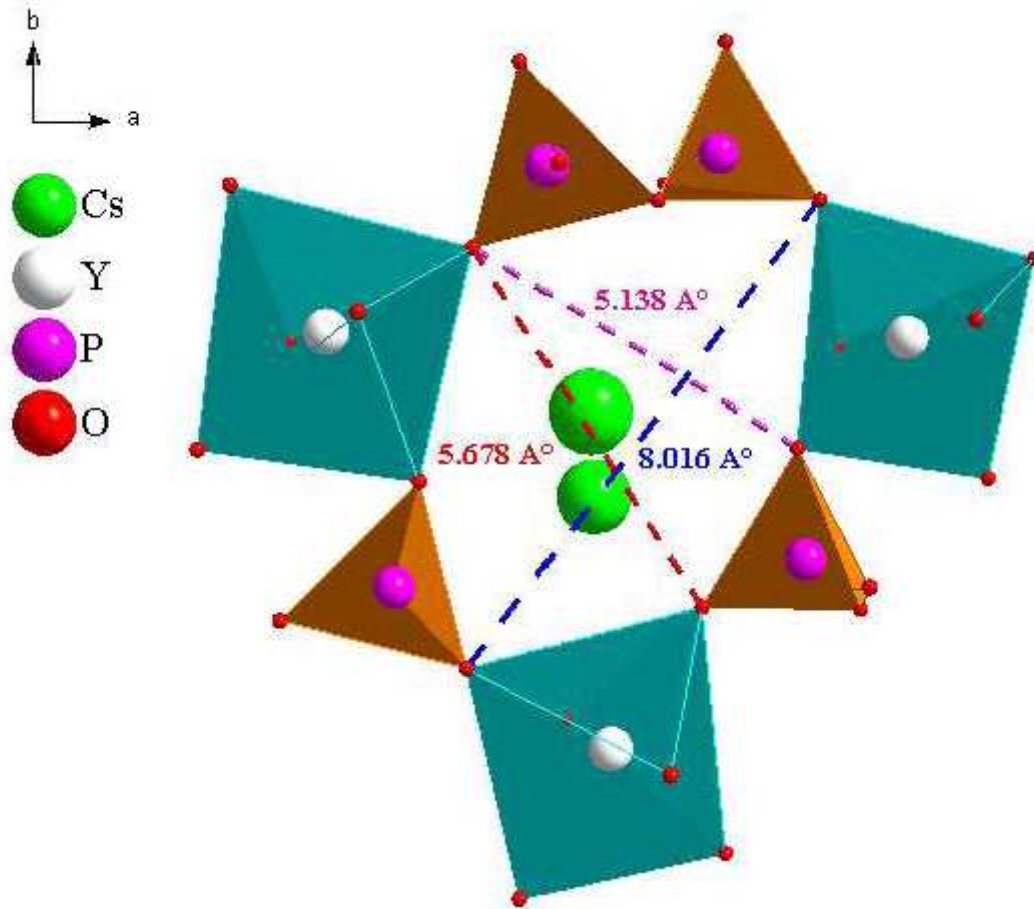


Figure 10

View of the shape and size of the [001] tunnel sections

Figure 11

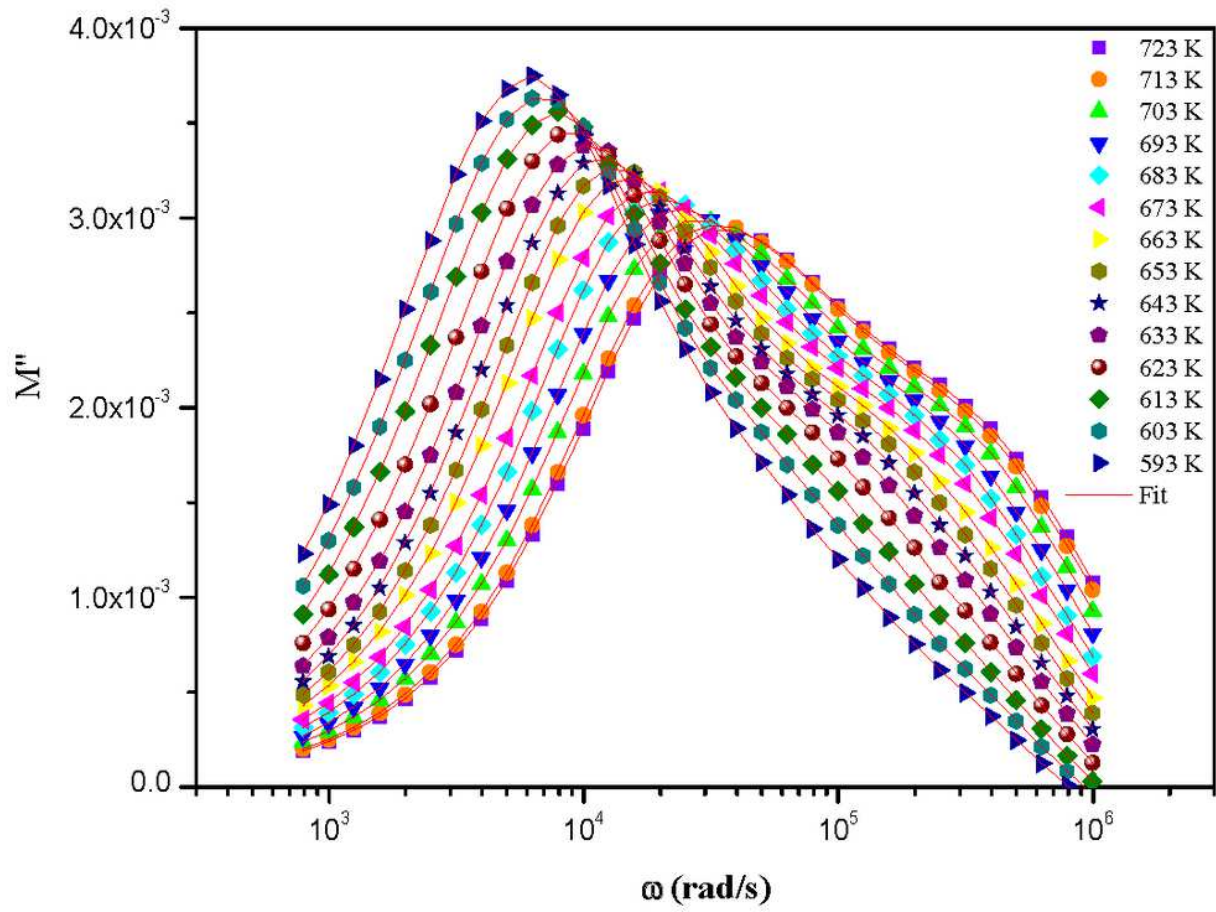


Figure 11

Imaginary part of the electrical modulus of the CsYP207

Figure 12

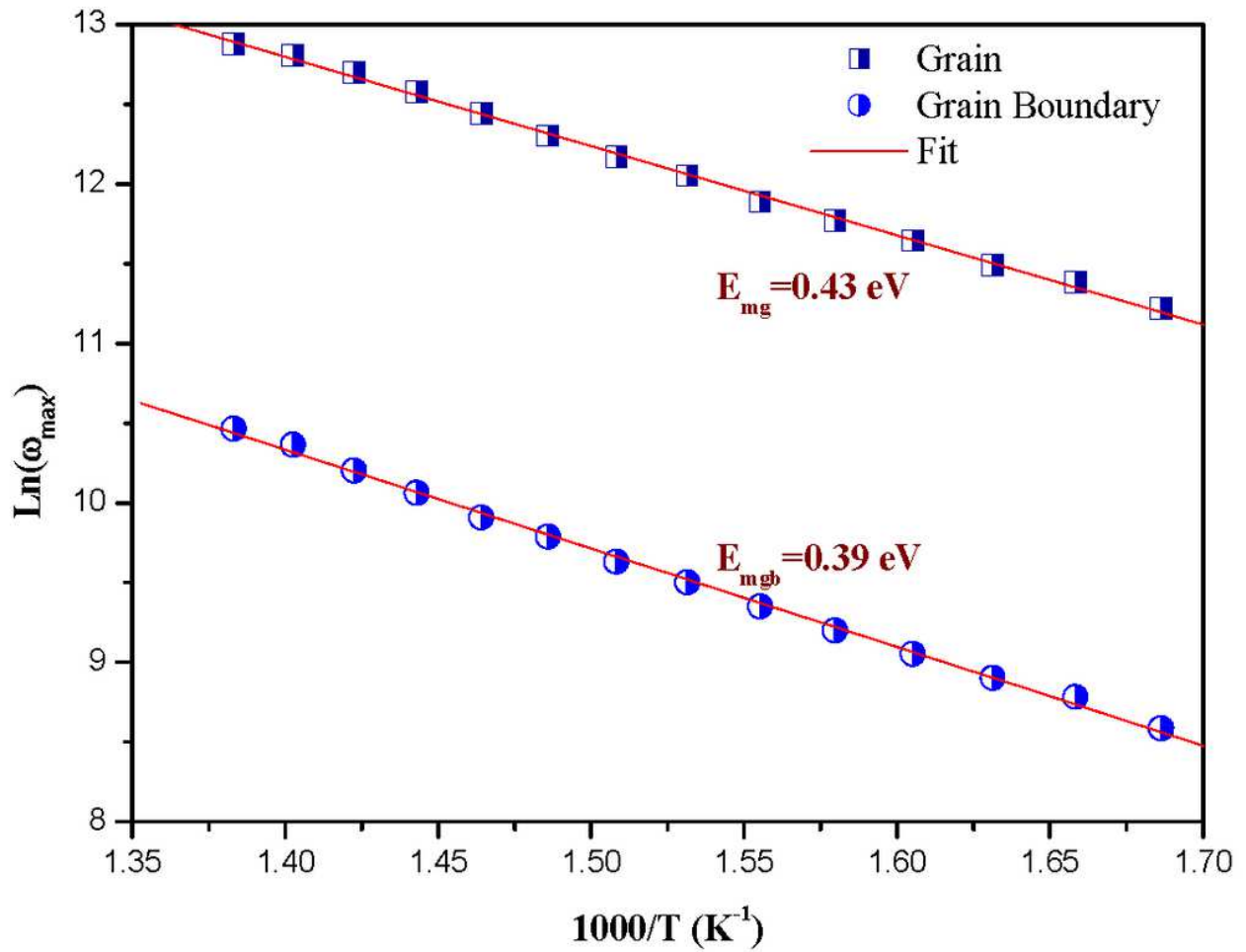


Figure 12

Temperature dependence of M''_{max}

Figure 13

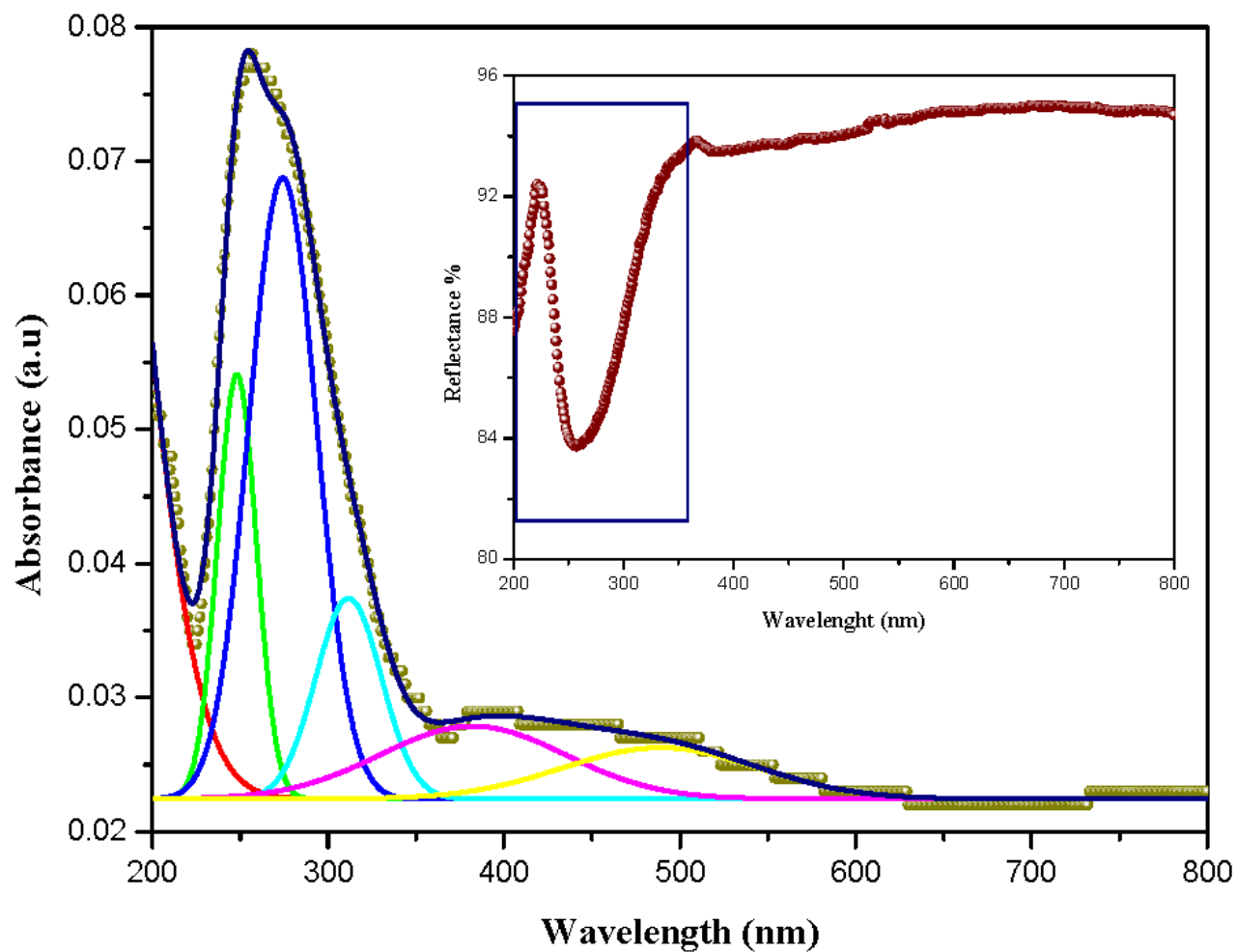


Figure 13

The absorbance and reflectance spectra for CsYP207 compound

Figure 14

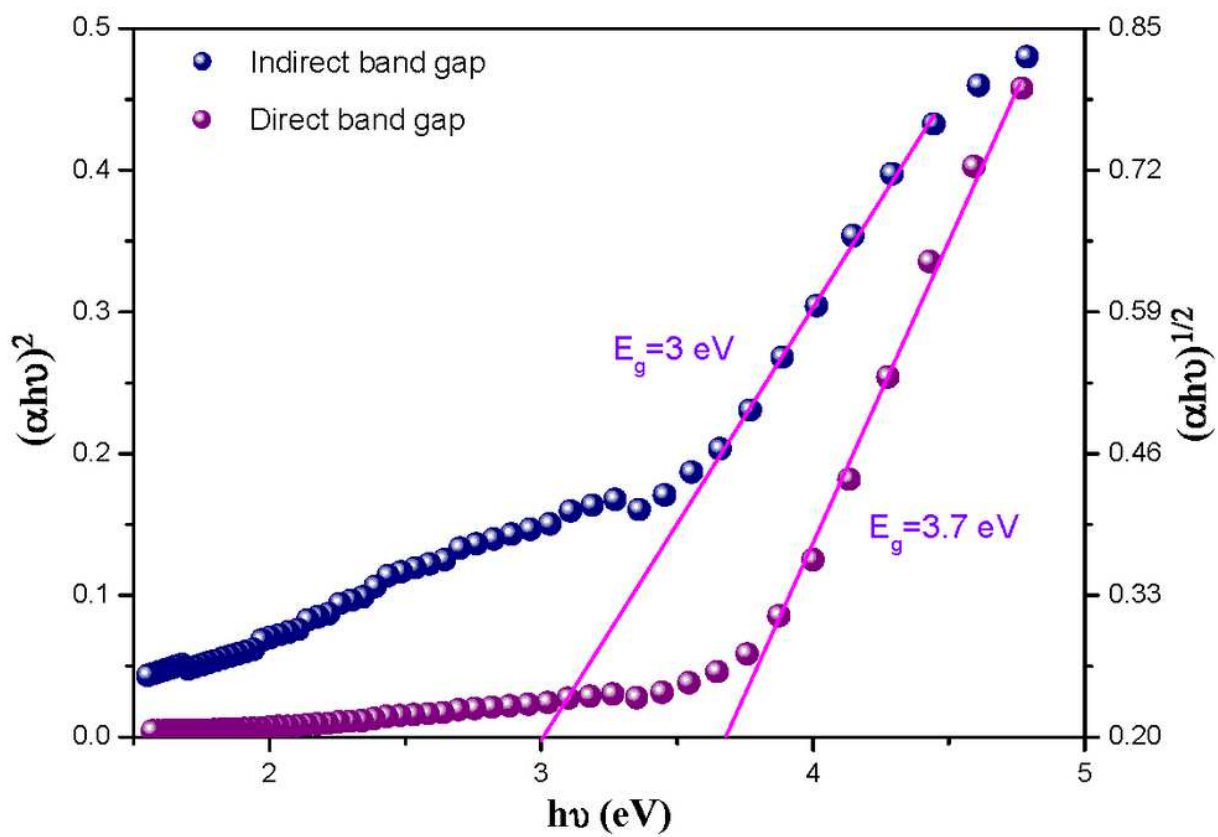


Figure 14

Dependence of $(\alpha h\nu)^2$ and $(\alpha h\nu)^{1/2}$ on the photon energy of CsYP207 compound.

Figure 15

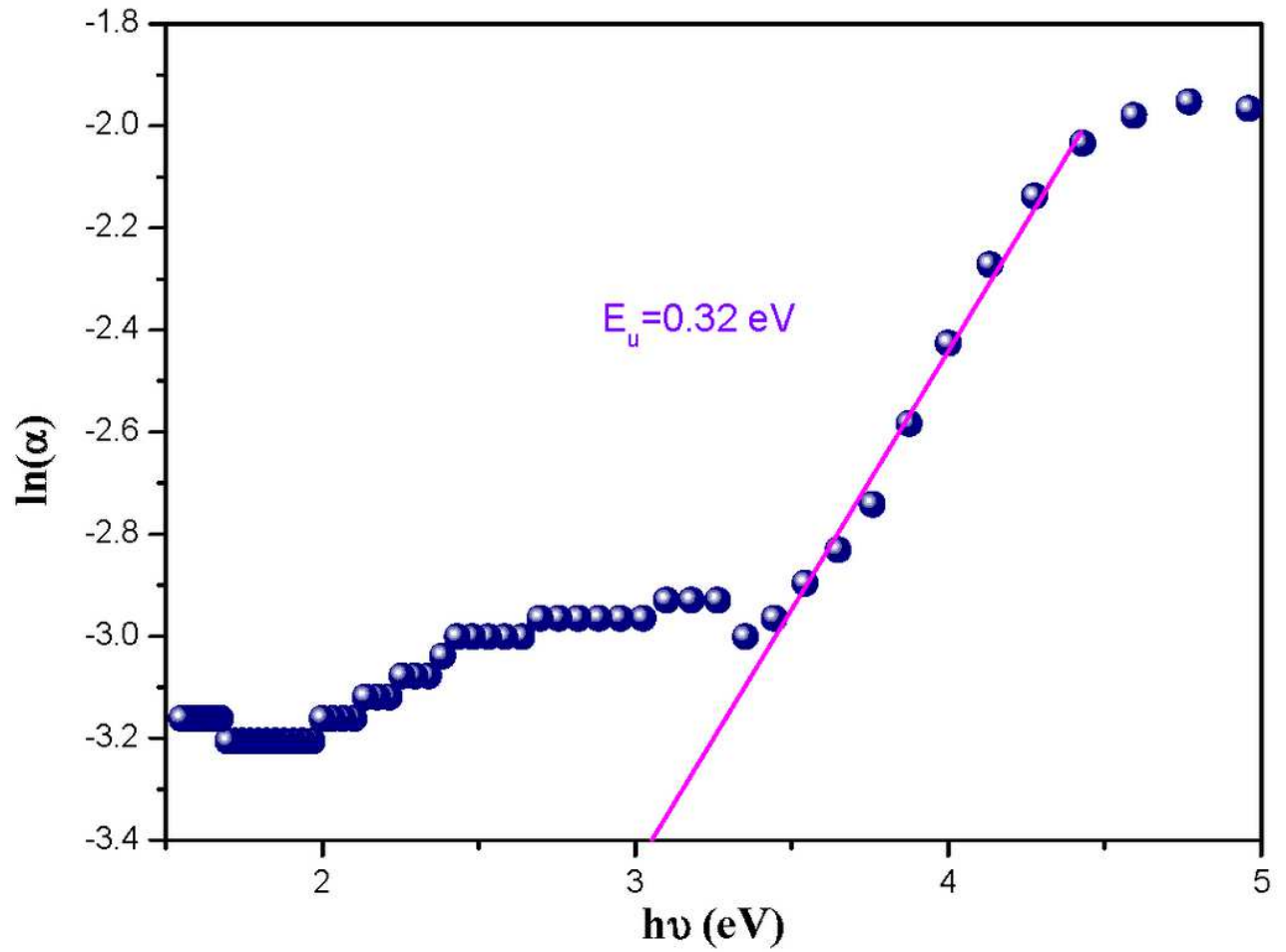


Figure 15

The logarithmic variation of the absorption coefficient versus photon energy